Rapid Communications | Editors' Suggestion

Photoinduced dynamics of nematic order parameter in FeSe

T. Konstantinova,[1,2] L. Wu,[1] M. Abeykoon,[1] R. J. Koch,[1] A. F. Wang,[1,*] R. K. Li,[3] X. Shen,[3] J. Li,[1] J. Tao,[1] I. A. Zaliznyak,[1] C. Petrovic,[1] S. J. L. Billinge,[1,4] X. J. Wang,[3] E. S. Bozin,[1] and Y. Zhu[1,2,†]

[1]*Brookhaven National Laboratory, Upton, New York 11973, USA*
[2]*Stony Brook University, Stony Brook, New York 11794, USA*
[3]*SLAC National Accelerator Laboratory, Menlo Park, California 94025, USA*
[4]*Columbia University, New York, New York 10027, USA*

(Received 24 February 2019; revised manuscript received 1 May 2019; published 28 May 2019)

Formation of electronic nematicity is a common thread of unconventional superconductors. We use ultrafast electron diffraction to probe the lattice interactions with electronic degrees of freedom in superconducting FeSe and find a significant lattice response to local nematicity. We observe that a perturbation by a laser pulse leads to a surprising enhancement of the high-symmetry crystalline order as a result of suppression of low-symmetry local lattice distortions, which are signatures of nematic fluctuations. The distortions are present at temperatures both below and above the nematic phase transition, as corroborated by our x-ray pair distribution function analysis and transmission electron microscopy measurements. Nonequilibrium lattice behavior of FeSe reveals two distinct time scales of nematic response to photoexcitation, 130(20) and 40(10) ps, corresponding to diffusive and percolative dynamics of nematic fluctuations respectively.

DOI: 10.1103/PhysRevB.99.180102

FeSe is the simplest iron-chalcogenide superconducting compound. In a common trend with other Fe-based superconductors (FBSCs), at low temperature FeSe undergoes a transition to the nematic electronic state, deemed a precursor of superconductivity, which is accompanied by a weak change in the average crystal symmetry from tetragonal $P4/nmm$ to orthorhombic $Cmma$ group. The origin of nematicity is still under debate [1], with spin [2], orbit [3], and charge fluctuations [4] considered as main mediators. Antiferromagnetic order, which usually closely follows the transition to the nematic state in iron pnictides, supports the spin scenario as a leading contender for the nematic order. FeSe, however, lacks a long-range magnetic order whereas localized spin fluctuations with subpicosecond time scales are observed [5,6], suggesting a quantum nematic paramagnet as its ground state [6] and attracting attention to local nematicity. Hence, FeSe presents a unique opportunity for the investigation of the formation of nematic order, dynamics of nematic fluctuations, and their relation to dynamical magnetism and nonconventional superconductivity.

The connection between the crystal lattice and electronic nematicity in FBSC is often neglected because of the apparently insignificant change of the unit-cell parameters in the nematic phase. In FeSe, a tetragonal-to-orthorhombic transition leads to only 0.5% distortion in the ab plane [7]. Nevertheless, there is growing evidence of coupling between the lattice and electronic degrees of freedom in this material. It includes sensitivity of superconducting temperature T_c and structural transition temperature T_S to pressure [8] and lattice strain [9], isotope effect [10], optical-phonon anomaly [11], phonon softening [12], and enhancement of T_c in a single layer FeSe on $SrTiO_3$ substrate [13,14] and in FeSe crystals with spacer layers [15].

In this work, we use ultrafast electron diffraction (UED) to investigate the dynamics of structural changes following the photoinduced melting of the nematic order in FeSe. We also present a detailed study of the local crystal structure of FeSe using pair distribution function (PDF) analysis of x-ray powder diffraction (XPD) and transmission electron microscopy (TEM). Our experiments reveal a surprising increase of crystallinity upon melting of low-symmetry nematic order and local lattice distortions, which we associate with local nematicity [16–19]. The distortions are present in both long-range nematic (orthorhombic) and normal (tetragonal) states, however, their correlation length increases below T_S. Upon photoexcitation, the distortions are released at two distinct rates, governed by percolative and diffusive dynamics of nematic fluctuations.

Single FeSe crystals were grown by the chemical vapor transport method using a eutectic mix of the KCl and $AlCl_3$ as the transport agent [20,21]. UED measurements were performed at MeV-UED setup at SLAC National Accelerator Laboratory. The details of the UED setup are described elsewhere [22]. XPD measurements for PDF analysis were performed at the PDF (28-ID-1) beamline of National Synchrotron Light Source–II at Brookhaven National Laboratory. High-resolution XPD data were obtained at the 11-BM beamline at the Advanced Photon Source at Argonne National Laboratory. TEM measurements including diffraction and imaging were performed at BNL using a 200-keV JEOL ARM 200 CF Microscope with a probe and an imaging aberration corrector.

UED provides information about the lattice dynamics in the system driven out-of-equilibrium with a pump laser pulse

*Present address: School of Physics, Chongqing University, Chongqing 400044, China.
†zhu@bnl.gov

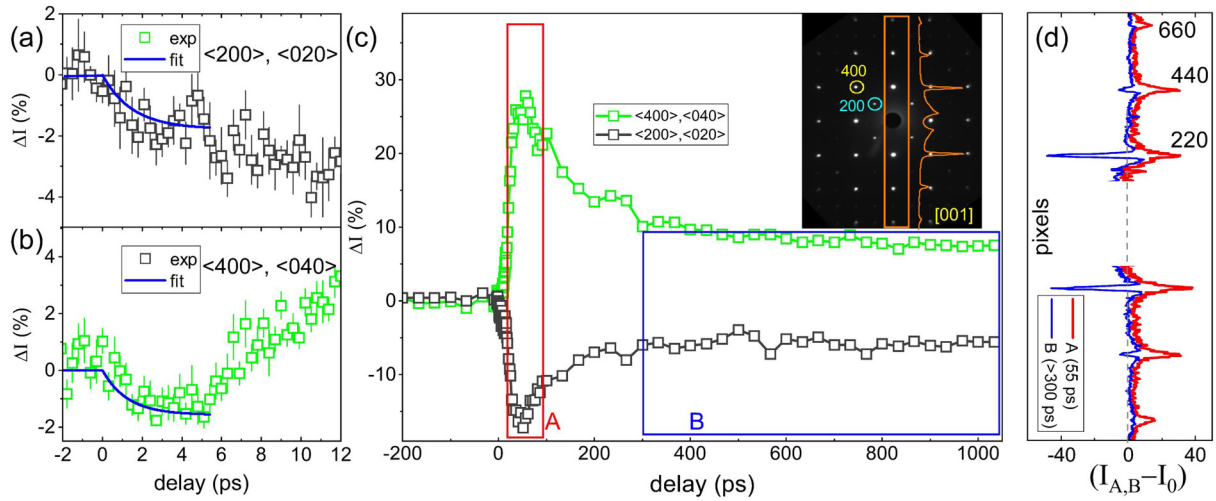

FIG. 1. Decay of the Bragg intensity during the first 5 ps for ⟨200⟩, ⟨020⟩ (a) and ⟨400⟩, ⟨040⟩ (b) reflections measured with UED at 27 K at fluence 1.24 mJ/cm^2. Solid blue curves are exponential decay fits for the experimental data. (c) The peaks' dynamics during 1000 ps. Inset shows the FeSe diffraction pattern. The orange line in the inset shows the diffraction intensity profile integrated within the indicated frame. Frames A (red) and B (blue) show the time regions where averaged intensity differences (d) were calculated. (d) Changes of the intensity profile, shown in the inset (c), after the pump pulse with respect to the profile of the unpumped sample. Red (blue) line corresponds to changes averaged over the time frame A (B) highlighted in (c).

and probed by an electron beam. We use 1.55-eV 60-fs photon pulses to excite electronic transitions in FeSe samples at temperatures from 27 to 300 K. To get information about the lattice response we focus first on the intensity changes of the Bragg reflections that can be related to the lattice symmetry changes. Typical intensity dynamics of ⟨200⟩, ⟨020⟩ and ⟨400⟩, ⟨040⟩ at 27 K are shown in Fig. 1 (we use *Cmma* symmetry for indexing peaks, unless stated otherwise). During the first 5 ps the intensities of all observable peaks go down by a few percent of the initial equilibrium values [Figs. 1(a) and 1(b)]. At this time scale, the intensity dynamics can be fitted with a single exponential decay with a time constant of 1.5–2 ps. Such behavior is consistent with the energy transfer from the excited electrons to the lattice through electron-phonon coupling, leading to the increase of atomic Debye-Waller factors. Similar time constants were observed for the initial recovery of electronic states in the time-resolved reflectivity experiments [19] for the same material and were also attributed to the electron-phonon coupling.

Beyond the first 5 ps the dynamics of the Bragg reflections are rather unusual. The intensities of the ⟨hk0⟩ Bragg peaks with $h + k = 4n + 2$ continue to drop for about 50 ps and then slowly recover. On the other hand, the intensities of the rest of the peaks ($h + k = 4n$) increase well above the initial values within the same 50 ps, before recovery. The rise of the intensity in this interval can be approximated [23] with a stretched exponential function (exponent $\beta = 2.6$) with time constant 40 ± 10 ps. The rate is similar to the rate of the photoinduced orthogonal-to-tetragonal phase transition in $BaFe_2As_2$ observed [24] with time-resolved x-ray diffraction. However, structural changes associated with such transition cannot lead to the observed intensity variations in the present experiment.

Consider the tetragonal 220 peak that splits into the orthorhombic 400 and 040 peaks. Such splitting is too small to be observed by UED since the experimental widths of the Bragg peaks are several times larger than the expected splitting. Assuming the high-symmetry positions of Fe and Se atoms obtained from the Rietveld refinements, the structure factors of these peaks, which determine their intensities in a thin sample, have an identical form,

$$SF_{220}^{\text{tetr}} = SF_{040}^{\text{orth}} = 4f_{\text{Se}}\exp(-B_{\text{Se}}) + 4f_{\text{Fe}}\exp(-B_{\text{Fe}}), \quad (1)$$

where $f_{\text{Se}}(f_{\text{Fe}})$ and $B_{\text{Se}}(B_{\text{Fe}})$ are the atomic form factor and the Debye-Waller factor for Se (Fe) atoms respectively. From Eq. (1) one can see that not only the transition between the two phases does not lead to an intensity change, but that no modification of atomic positions could increase the intensity of ⟨040⟩ (and other $h + k = 4n$) peaks because for those reflections the electrons already scatter in-phase from all atoms in the unit cell. An apparent intensity increase suggests that some lattice distortions *pre-exist* at equilibrium, yielding a reduced Bragg intensity compared to the ideal structure factor of Eq. (1). In such case, a photodriven release of these distortions results in the intensity rise.

A closer look at the shape of the diffraction peaks provides additional information about the lattice dynamics. The inset in Fig. 1(c) shows the intensity profile integrated along the [110] direction. Changes in the profile [Fig. 1(d)] at time delays around +55 ps and beyond +300 ps show that the integrated intensity of $h + k = 4n$ peaks increases. However, changes at peaks' centers are different from changes at peaks' tails. A separation of an individual peak's profile into a narrow Gaussian part, corresponding to the long-range crystal order, and a wider Lorentzian part, corresponding to a short-range order [23] shows that the lattice dynamics involve three major steps. First, the photoinduced atomic vibrations lead to the decrease of the Bragg peaks' intensity, which is transferred to the thermal diffuse background. Second, the release of the pre-existing distortions, which in the absence of photoexcitation give rise to a broad diffuse scattering near $q = 0$, induces the recrystallization of the high-symmetry phase, i.e., causes

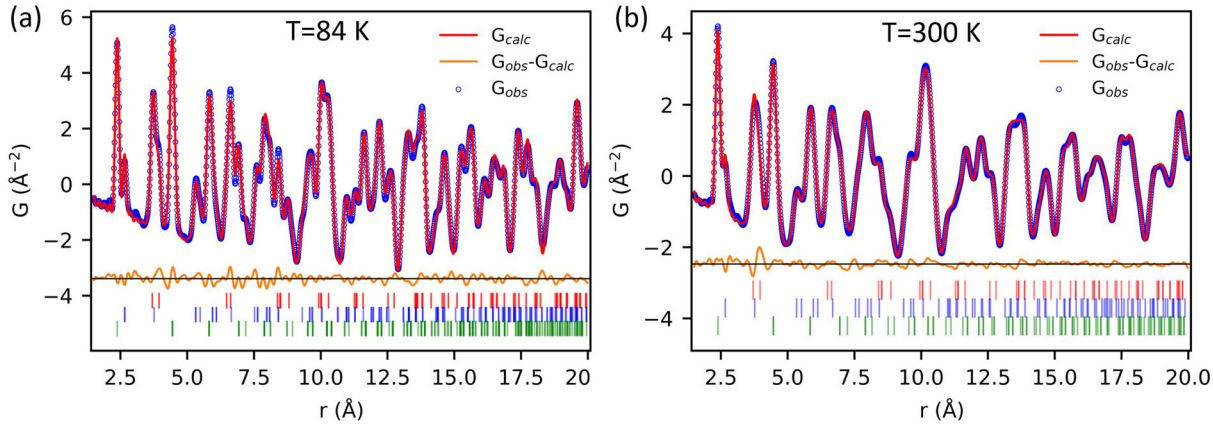

FIG. 2. (a) PDF at 84 K with the fit assuming an orthorhombic structural model. (b) PDF at 300 K with the fit assuming a tetragonal structural model. Blue circles show the experimental data, red line is the fit to the respective model, orange line shows the misfit. The plots contain green (Fe-Se), blue (Fe-Fe), and red (Se-Se) tick marks below the residual, which indicate the different unique pair distances from refining the respective models.

changes in the average crystal structure (long-range order) by moving atoms to more symmetric positions. This displacive process leads to an increase (decrease) of structure factors for $h + k = 4n (h + k = 4n + 2)$ peaks. The behavior of the Gaussian component is determined by the combination of vibrational and displacive effects. Third, the melting of the local distortions also creates tiny domains of high-symmetry phase, increasing the intensity of the Lorentzian component. The size of the domains determines the width of the Lorentzian component and can be estimated around 15–20 Å.

The crystal lattice in S-doped samples photoexcited under comparable conditions demonstrates a similar response [23], pointing out that the distortions are common for at least a part of the $FeSe_{1-x}S_x$ phase diagram. To understand the nature of these pre-existing local distortions, breaking the lattice symmetry at equilibrium, we turn to static techniques such as XPD and TEM.

Atomic displacements corresponding to the bond disparity of 0.1 Å have been observed in $Fe_{1+y}Te$, where they were attributed to a long-range ferro-orbital ordering [25]. To search for similar atomic displacements in FeSe, we performed pair distribution function analysis of the XPD data. PDF contains information about both long-range order and local imperfections, which is inferred from the powder-diffraction pattern. Figure 2(a) shows PDF data at $T = 84$ K together with the fit to an orthorhombic model, obtained from the Rietveld refinement. Whereas the model describes the data well at large interatomic distances r, for $r < 10$ Å there is a notable misfit. The misfit indicates that there is a disparity between the local and average atomic structure and corroborates the assumption that lattice distortions are present at equilibrium.

Remarkably, a pronounced misfit to the tetragonal model at small interatomic distances is also present at 300 K [Fig. 2(c)]. Thus, the local lattice distortions also exist in the tetragonal phase. The deviation from the tetragonal model is most pronounced for the lattice repeat peak at $r = 3.8$ Å and rapidly fades at larger r, indicating a short correlation length. The information about the distortions in PDF comes not from the Bragg peaks, but from diffuse scattering. It agrees with the UED observations, where melting of the distortions involves intensity transfer from the diffuse background centered at $q = 0$ to locations at or near Bragg peaks. The exact structure of the distortions and the growth of the distortion's correlation length at low temperature are described elsewhere [26,27]. Neutron powder-diffraction experiments in other FBSCs have also observed [28,29] local structures that are different from the average ones. In $BaFe_2As_2$ such distortions were suggested [29] to reduce the amplitude of the long-range magnetic moment.

Whereas XPD provides structural information averaged over multiple lattice domains, TEM is a local probe and presents an opportunity to look at individual domains and to reconstruct the details that could be missed upon averaging under a large probe. The results of our TEM measurements of FeSe samples are shown in Fig. 3. The Bragg peaks in the diffraction obtained from the sample are sharp and without streaks, indicating a good sample quality. In agreement with the previous studies on FeSe [7] and LaOFeAs [30], $\langle 110 \rangle$ peaks forbidden by *Cmma* symmetry appear in the diffraction pattern below T_S (at $T = 88$ K) [Figs. 3(a) and 3(b)] whereas they are not seen at the same sample area at $T = 300$ K. The peaks indicate that the crystal symmetry below T_S is lower than *Cmma*. Such peaks were not detected in the XPD measurements [23].

Figure 3(c) shows a high-resolution TEM (HRTEM) image obtained at 300 K with a smaller field of view than is used for the diffraction measurements. Fourier analysis of such images [Fig. 3(d)] reveals nonuniformly distributed regions whose diffractograms have a pair of forbidden peaks (either $\bar{1}10$ and $1\bar{1}0$ or 110 and $\bar{1}\bar{1}0$), or a full set of four $\langle 110 \rangle$ peaks in addition to the peaks allowed by *Cmma* or $P4/nmm$ symmetry [23]. Yet other regions have only allowed peaks. Appearance of the peaks in either of the two diagonal directions in diffractograms can be explained by presence of domains with C_2 symmetry in the *ab* plane, which are rotated by 90° with respect to each other. The difference in the forbidden peaks' intensities along the perpendicular directions of the diffraction pattern at 88 K [23] also supports the idea of rotated domains with C_2 symmetry below T_S, which are nonequally present in the probed volume. The inverse Fourier transform mapping [23] reveals that at 300 K the domains with the low symmetry have a typical size of 1–5 nm. This is to be contrasted with

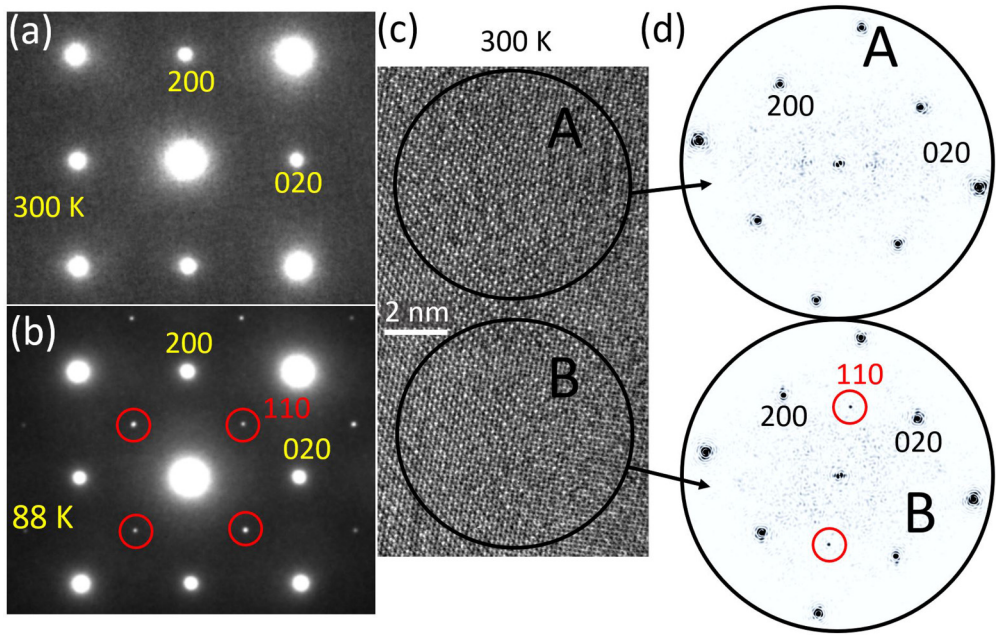

FIG. 3. (a) Electron-diffraction pattern at 300 K (b) Electron diffraction from the same area as (a) at 88 K. (c) Typical HRTEM image. (d) FFTs taken from the respective areas as shown in (c). The peaks forbidden by the orthorhombic and tetragonal symmetries are highlighted by red circles.

the crystalline domain size observed by XPD, which is about 200 nm, highlighting the distinction between the reduced symmetry domains and crystallites. Appearance of the sharp ⟨110⟩ peaks in the electron diffraction below T_S indicates that the low-symmetry domain size grows upon lowering the temperature, consistent with the behavior of the correlation length of the local distortions revealed with the PDF analysis. These observations corroborate that even at 300 K the sample has regions with the broken tetragonal symmetry, where either or both atoms in the unit cell are displaced from the high-symmetry positions, leading to the atomic bond disparity. The disparity agrees with the misfit of the PDF model described above.

The photoinduced FeSe lattice dynamics at different temperatures provide important information about changes in the system across the nematic phase transition. As shown in Fig. 4(a), the relatively fast (within 50 ps) increase of ⟨080⟩, ⟨800⟩ peaks intensity, corresponding to the release of the distortions, is only observed at temperatures below T_S. Above T_S the intensity rises as well, however at a much slower rate, and can be described with exponential growth function with the time constant of 130 ± 20 ps. The photoinduced increase of intensity above T_S agrees with the presence of local nematic distortions observed with x ray and TEM. Remarkably, the relative intensity at 1-ns delay seems to be independent of temperature. For dynamics of other peaks refer to the Supplemental Material [23].

Fluence dependence [Fig. 4(b)] of the lattice dynamics at 27 K also reveals switching between the fast and the slow regimes. The fast component is observed only at fluences below 2.2 mJ/cm^2. The value of the maximum intensity first grows with fluence and then drops above 1.9 mJ/cm^2. Above

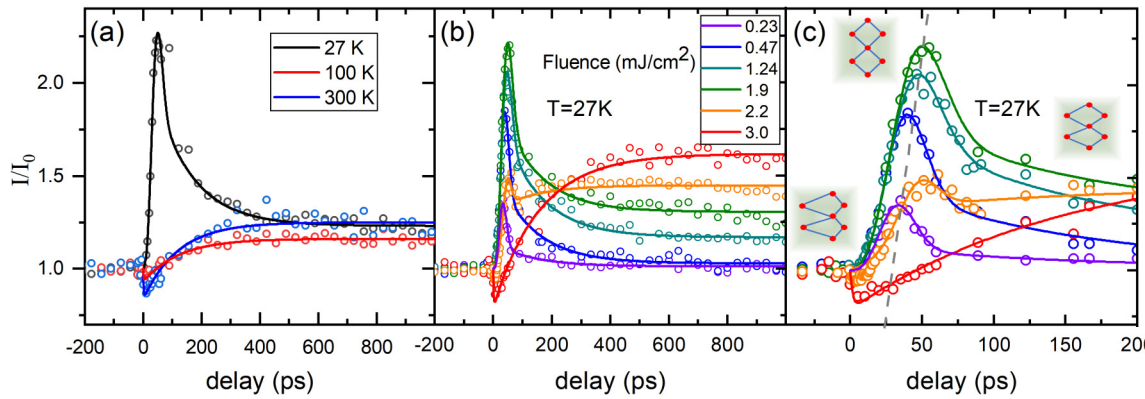

FIG. 4. (a) Dynamics of ⟨080⟩, ⟨800⟩ peaks obtained with UED at different temperatures for the incident fluence of 1.65 mJ/cm^2. Dynamics of the same peaks at different excitation fluences for the full measurement time range (b) and during the first 200 ps (c) at 27 K. The gray dashed line in (c) is a guide to eye. Insets show schematics of unequal atomic bonds at the corresponding time intervals. Open circles are the experimental data and solid lines are the fits [23].

$2.2\,\mathrm{mJ/cm^2}$ the lattice response is the same as at high sample temperature, i.e., the slow component is observed. This can be explained by the sample heating. Based on the sample characteristics [31,32], if all absorbed energy is converted to heat the threshold fluence corresponds to a temperature increase of 75 K, which is close to a 64-K difference between the sample temperature and T_S. Thus, the process leading to the fast increase of the peaks' intensity proceeds only in the presence of a (partial) long-range nematic order. When the order is destroyed, either by temperature or through above- threshold photoexcitation, the slow process governs the lattice dynamics. The slow process is also present at the low-temperature–low fluence excitation regime. Figure 4(c) shows that the point of the maximum intensity shifts to the longer time with increased fluence, reflecting the increased impact of the slow process. Thus, the slow and the fast responses "compete" with each other: as the laser fluence (or sample temperature) increases the slower process becomes more pronounced and finally dominant.

It is often believed that weak orthorhombicity of the unit cell is the only result of coupling between the electronic nematic order and the lattice in the FeSe superconducting family. Our observations reveal an additional connection, established via atomic bonds' distortions that lower the local lattice symmetry. Such distortions are present in nanodomains at temperatures both below and above T_S and correspond to local nematic fluctuations, consistent with previous observations [16,17,19]. Their correlation length increases as domain size grows on cooling, leading to the percolative three-dimensional ordering, i.e., lowering the average lattice symmetry, below T_S. This transition and the presence of the uncorrelated low-symmetry domains both below and above the ordering temperature agrees with the theoretical predictions of the anisotropic random field Ising model (ARFIM), which was argued to describe phase transitions with the discrete two-fold symmetry breaking in layered systems [33,34]. The ordering transition in this model occurs within the extended critical state where the domains of the two phases coexist, via formation of the percolating long-range order (LRO) domains.

A notable feature of the nonequilibrium lattice dynamics is the threshold excitation fluence at low temperatures, which corresponds to the energy needed to completely melt the long-range nematic order. Below the threshold fluence, i.e., when a partial nematic order parameter is still present after the excitation, the rate of the distortion release is relatively fast. The process reflects nucleation, growth, and merging of high-symmetry domains, i.e., percolative dynamics of the nematic order parameter. Similar rates of photoinduced LRO domain growth have been observed in other systems [35,36]. Newly formed large high-symmetry domains are unstable, and the distortions are formed again within few hundred picoseconds reflecting the recovery of the nematic phase [19,37]. Excitation above the threshold fluence results in a complete melting of the nematic order parameter via "overheating" the sample and leads to a slow relaxation of the lattice distortions, the same as observed at temperatures above T_S. Change of the distortion amplitude in the slow process depends only on the excitation fluence and not on the sample initial temperature. The process corresponds to establishing balance between domains of high and low symmetry through diffusive dynamics of the local nematic fluctuations. The recovery of the diffraction intensity following the rapid increase in the low fluence excitation regime proceeds on a time scale of about 80 ps, resulting from the combination of both the fast (percolative) and the slow (diffusive) dynamics of nematic fluctuations [23].

The structure of the dynamical magnetic correlations in FeSe and related Fe(Te,Se) materials is uniquely determined by local orbital overlaps, which are governed by nematic fluctuations [38]. However, the nematic time scales observed in our experiments are orders of magnitude longer than those for spin fluctuations in FeSe [5,6], clearly indicating that nematic order is the parent phase, rather than the consequence of dynamical magnetism in this material.

In summary, our study reveals dynamical dichotomy of nematic fluctuations in FeSe. In the ordered phase and at low photon fluencies, UED observes a fast ($\tau_{\mathrm{fast}} = 40 \pm 10$ ps) structural response with stretched-exponential ($\beta = 2.6 \pm 0.1$) relaxation. This is not unexpected for the percolation-type dynamics in an effective Ising model predicted by the ARFIM [33,34], which governs melting of the low-symmetry phase with nematic LRO and leads to the increase of Bragg peaks characteristic of the high-symmetry phase. We also find a slow ($\tau_{\mathrm{slow}} = 130 \pm 20$ ps) exponential relaxation process, which corresponds to the diffusive intrinsic dynamics of short-range nematic fluctuations in FeSe. These are revealed as nanodomains with local low-symmetry lattice distortions that couple to the electronic degrees of freedom. Using UED, we observe melting of these nematic nanodomains following a femtosecond laser pulse and the concomitant lattice ordering of the high-symmetry parent phase resulting in a surprising increase of coherent Bragg scattering. The pre-existing local distortions are present at equilibrium both in the absence of nematic LRO and in the ordered phase and their existence can be understood from the ARFIM. The ARFIM phase diagram predicts the domains of both low- and high-symmetry phases below and above the percolative phase transition [39,40]. The observed structural response, which is naturally explained by redistribution of the relative population of the two phases, sheds light on the formation of the nematic phase from imperfect ordering of its fluctuations in FeSe and other layered systems and stimulates further theoretical development towards full understanding of nematicity.

The authors thank A. F. Kemper, L. Classen, A. V. Chubukov, R. M. Konik, and A. M. Lindenberg for useful discussions and S. Lapidus for XPD measurements at the 11-BM beamline at APS. This research used the 28-ID-1 (PDF) beamline of the National Synchrotron Light Source II and the JEOL ARM 200 CF Microscope at BNL. Work at Brookhaven National Laboratory was supported by US Department of Energy (DOE), Office of Science, Office of Basic Energy Sciences (BES), Materials Science and Engineering Division under Contract No. DE-SC0012704. The UED work was performed at SLAC MeV-UED, which is supported in part by the DOE BES Scientific User Facilities Division Accelerator & Detector R&D program, the LCLS Facility, and SLAC under Contracts No. DE-AC02-05-CH11231 and No. DE-AC02-76SF00515.

[1] R. M. Fernandes, A. V. Chubukov, and J. Schmalian, Nat. Phys. **10**, 97 (2014).

[2] C. Fang, H. Yao, W. F. Tsai, J. P. Hu, and S. A. Kivelson, Phys. Rev. B **77**, 224509 (2008).

[3] S. H. Baek, D. V. Efremov, J. M. Ok, J. S. Kim, J. van den Brink, and B. Buchner, Nat. Mater. **14**, 210 (2015).

[4] P. Massat, D. Farina, I. Paul, S. Karlsson, P. Strobel, P. Toulemonde, M. A. Measson, M. Cazayous, A. Sacuto, S. Kasahara, T. Shibauchi, Y. Matsuda, and Y. Gallais, Proc. Natl. Acad. Sci. USA **113**, 9177 (2016).

[5] T. Imai, K. Ahilan, F. L. Ning, T. M. McQueen, and R. J. Cava, Phys. Rev. Lett. **102**, 177005 (2009).

[6] Q. S. Wang, Y. Shen, B. Y. Pan, X. W. Zhang, K. Ikeuchi, K. Iida, A. D. Christianson, H. C. Walker, D. T. Adroja, M. Abdel-Hafiez, X. J. Chen, D. A. Chareev, A. N. Vasiliev, and J. Zhao, Nat. Commun. **7**, 12182 (2016).

[7] T. M. McQueen, A. J. Williams, P. W. Stephens, J. Tao, Y. Zhu, V. Ksenofontov, F. Casper, C. Felser, and R. J. Cava, Phys. Rev. Lett. **103**, 057002 (2009).

[8] S. Medvedev, T. M. McQueen, I. A. Troyan, T. Palasyuk, M. I. Eremets, R. J. Cava, S. Naghavi, F. Casper, V. Ksenofontov, G. Wortmann, and C. Felser, Nat. Mater. **8**, 630 (2009).

[9] S. H. Baek, D. V. Efremov, J. M. Ok, J. S. Kim, J. van den Brink, and B. Buchner, Phys. Rev. B **93**, 180502(R) (2016).

[10] R. Khasanov, M. Bendele, K. Conder, H. Keller, E. Pomjakushina, and V. Pomjakushin, New J. Phys. **12**, 073024 (2010).

[11] M. Nakajima, K. Yanase, F. Nabeshima, Y. Imai, A. Maeda, and S. Tajima, Phys. Rev. B **95**, 184502 (2017).

[12] K. Zakeri, T. Engelhardt, T. Wolf, and M. Le Tacon, Phys. Rev. B **96**, 094531 (2017).

[13] J. F. Ge, Z. L. Liu, C. H. Liu, C. L. Gao, D. Qian, Q. K. Xue, Y. Liu, and J. F. Jia, Nat. Mater. **14**, 285 (2015).

[14] W. W. Zhao, M. D. Li, C. Z. Chang, J. Jiang, L. J. Wu, C. X. Liu, J. S. Moodera, Y. M. Zhu, and M. H. W. Chan, Sci. Adv. **4**, eaao2682 (2018).

[15] M. Burrard-Lucas, D. G. Free, S. J. Sedlmaier, J. D. Wright, S. J. Cassidy, Y. Hara, A. J. Corkett, T. Lancaster, P. J. Baker, S. J. Blundell, and S. J. Clarke, Nat. Mater. **12**, 15 (2013).

[16] P. S. Wang, P. Zhou, S. S. Sun, Y. Cui, T. R. Li, H. C. Lei, Z. Q. Wang, and W. Q. Yu, Phys. Rev. B **96**, 094528 (2017).

[17] Y. C. Wen, K. J. Wang, H. H. Chang, J. Y. Luo, C. C. Shen, H. L. Liu, C. K. Sun, M. J. Wang, and M. K. Wu, Phys. Rev. Lett. **109**, 089902(E) (2012).

[18] K. Nakayama, Y. Miyata, G. N. Phan, T. Sato, Y. Tanabe, T. Urata, K. Tanigaki, and T. Takahashi, Phys. Rev. Lett. **113**, 237001 (2014).

[19] C.-W. Luo, P. Chung Cheng, S.-H. Wang, J.-C. Chiang, J.-Y. Lin, K.-H. Wu, J.-Y. Juang, D. A. Chareev, O. S. Volkova, and A. N. Vasiliev, npj Quantum Mater. **2**, 32 (2017).

[20] R. W. Hu, H. C. Lei, M. Abeykoon, E. S. Bozin, S. J. L. Billinge, J. B. Warren, T. Siegrist, and C. Petrovic, Phys. Rev. B **83**, 224502 (2011).

[21] D. Chareev, E. Osadchii, T. Kuzmicheva, J. Y. Lin, S. Kuzmichev, O. Volkova, and A. Vasiliev, CrystEngComm **15**, 1989 (2013).

[22] S. P. Weathersby, G. Brown, M. Centurion, T. F. Chase, R. Coffee, J. Corbett, J. P. Eichner, J. C. Frisch, A. R. Fry, M. Guhr, N. Hartmann, C. Hast, R. Hettel, R. K. Jobe, E. N. Jongewaard, J. R. Lewandowski, R. K. Li, A. M. Lindenberg, I. Makasyuk, J. E. May *et al.*, Rev. Sci. Instrum. **86**, 073702 (2015).

[23] See Supplemental Material at http://link.aps.org/supplemental/10.1103/PhysRevB.99.180102 for a detailed analysis which also includes Refs. [19,20,24,37,41,42].

[24] L. Rettig, S. O. Mariager, A. Ferrer, S. Grubel, J. A. Johnson, J. Rittmann, T. Wolf, S. L. Johnson, G. Ingold, P. Beaud, and U. Staub, Struct. Dyn. **3**, 023611 (2016).

[25] D. Fobes, I. A. Zaliznyak, Z. J. Xu, R. D. Zhong, G. D. Gu, J. M. Tranquada, L. Harriger, D. Singh, V. O. Garlea, M. Lumsden, and B. Winn, Phys. Rev. Lett. **112**, 187202 (2014).

[26] R. J. Koch, T. Konstantinova, M. Abeykoon, A. F. Wang, C. Petrovic, Y. Zhu, E. S. Bozin, and S. J. L. Billinge, arXiv:1902.08732.

[27] B. A. Frandsen, Q. Wang, S. Wu, J. Zhao, and R. J. Birgeneau, arXiv:1904.06440.

[28] B. A. Frandsen, K. M. Taddei, M. Yi, A. Frano, Z. Guguchia, R. Yu, Q. M. Si, D. E. Bugaris, R. Stadel, R. Osborn, S. Rosenkranz, O. Chmaissem, and R. J. Birgeneau, Phys. Rev. Lett. **119**, 187001 (2017).

[29] J. L. Niedziela, M. A. McGuire, and T. Egami, Phys. Rev. B **86**, 174113 (2012).

[30] C. Ma, L. J. Zeng, H. X. Yang, H. L. Shi, R. C. Che, C. Y. Liang, Y. B. Qin, G. F. Chen, Z. A. Ren, and J. Q. Li, Europhys. Lett. **84**, 47002 (2008).

[31] X. J. Wu, D. Z. Shen, Z. Z. Zhang, J. Y. Zhang, K. W. Liu, B. H. Li, Y. M. Lu, B. Yao, D. X. Zhao, B. S. Li, C. X. Shan, X. W. Fan, H. J. Liu, and C. L. Yang, Appl. Phys. Lett. **90**, 112105 (2007).

[32] A. V. Muratov, A. V. Sadakov, S. Y. Gavrilkin, A. R. Prishchepa, G. S. Epifanova, D. A. Chareev, and V. M. Pudalov, Physica B: Condens. Matter **536**, 785 (2018).

[33] O. Zachar and I. Zaliznyak, Phys. Rev. Lett. **91**, 036401 (2003).

[34] I. A. Zaliznyak, Z. J. Xu, J. S. Wen, J. M. Tranquada, G. D. Gu, V. Solovyov, V. N. Glazkov, A. I. Zheludev, V. O. Garlea, and M. B. Stone, Phys. Rev. B **85**, 085105 (2012).

[35] M. Zhang, G. L. Cao, H. F. Tian, S. S. Sun, Z. W. Li, X. Y. Li, C. Guo, Z. Li, H. X. Yang, and J. Q. Li, Phys. Rev. B **96**, 174203 (2017).

[36] K. Haupt, M. Eichberger, N. Erasmus, A. Rohwer, J. Demsar, K. Rossnagel, and H. Schwoerer, Phys. Rev. Lett. **116**, 016402 (2016).

[37] A. Patz, T. Li, S. Ran, R. M. Fernandes, J. Schmalian, S. L. Bud'ko, P. C. Canfield, I. E. Perakis, and J. Wang, Nat. Commun. **5**, 3229 (2014).

[38] I. Zaliznyak, A. T. Savici, M. Lumsden, A. Tsvelik, R. W. Hu, and C. Petrovic, Proc. Natl. Acad. Sci. USA **112**, 10316 (2015).

[39] E. W. Carlson and K. A. Dahmen, Nat. Commun. **2**, 379 (2011).

[40] L. M. Nie, G. Tarjus, and S. A. Kivelson, Proc. Natl. Acad. Sci. USA **111**, 7980 (2014).

[41] T. M. McQueen, Q. Huang, V. Ksenofontov, C. Felser, Q. Xu, H. Zandbergen, Y. S. Hor, J. Allred, A. J. Williams, D. Qu, J. Checkelsky, N. P. Ong, and R. J. Cava, Phys. Rev. B **79**, 014522 (2009).

[42] E. J. Kirkland, *Advanced Computing in Electron Microscopy* (Springer, Boston, MA, 1998).